A Reconfigurable Microfluidic Building Block Platform for High-Throughput Nonhormonal Contraceptive Screening

Jyong-Huei Lee, [a] Carl van der Linden[b], Francisco J. Diaz[b*], and Pak Kin Wong [a,c*]

Identifying nonhormonal contraceptives will have profound impacts on avoiding side effects of hormonal birth control methods, minimizing pregnancy complications and infant mortality rates, and promoting family planning. However, phenotypic screening of contraceptives is challenging due to the diverse procedures associated with oocyte culture, biochemical assays, and molecular imaging. This study reports a multifunctional microfluidic platform comprising reconfigurable building blocks and interfaces to implement various cell-based drug screening protocols. This versatile platform has three major layers. The top layer consists of interchangeable 3D microfluidic building blocks (e.g., branching microchannels, chemical gradient generators, pumpless flow controllers, and emulsion generators) or an open interface. The middle layer incorporates a multiwell array with embedded membrane filters for live cell culture, medium exchange, enzymatic cumulus cell removal, washing, and fluorescence staining. The bottom layer is also reconfigurable for waste collection, oocyte culture, plate reader measurement, and high-resolution microscopy. We demonstrate an 8 by 16 (128 well) system for performing the cumulus-oocyte complex (COC) expansion and oocyte maturation assays for screening nonhormonal contraceptives. The microfluidic building block platform is scalable and can be reconfigured for a variety of drug screening applications in the future.

Introduction

Unintended pregnancy is associated with various maternal complications and infant morbidity and mortality [1]. Hormonal contraceptive drugs are currently the most common birth control method. However, hormonal methods can induce unwanted side effects, such as weight gain, irregular bleeding, mood change, and nausea [2-3], resulting in poor drug compliance. Identifying nonhormonal contraceptive compounds that inhibit COC maturation and expansion [4-7] may provide new opportunities to promote family planning and prevent unintended pregnancy, especially in developing countries. Nevertheless, high-throughput drug screening techniques, such as liquid handling robots and advanced microplate readers, are prohibitively expensive and complicated. More importantly, these platforms can often be ineffective in performing complicated procedures, such as the in situ culture, medium exchange, isolation, washing, and fluorescence staining steps, required in the COC maturation assay.

Microfluidics provides a promising strategy for addressing the unmet need in phenotypic contraceptive screening. Organs-on-chips devices mimic the in vivo microenvironment for cell-based drug screening [8]. Microfluidic chemical gradient generators allow testing of multiple drug concentrations simultaneously [9]. Digital microfluidics (e.g., electrowetting-on-dielectric and SLIPS-LAB) can manipulate liquid droplets to perform relatively complicated protocols and assays [10-11]. Multiphase microfluidics can generate a large number of emulsion droplets for parallel testing [12]. While cost effective and amendable for automation, these microfluidic systems typically have fixed designs and are incompatible with high-throughput drug screening procedures (e.g., loading drugs from compound libraries and high resolution imaging) [13-14]. There is often a trade-off between the flexibility and throughput in these systems (Figure 1A). It remains challenging to execute large scale phenotypic contraceptive screening with COCs.

Our team has previously demonstrated a membrane-based microfluidic device with aqueous-oil interfaces for studying COC maturation [15]. However, the design has an inflexible single input inlet, can accommodate only a linear array, and is incompatible with high resolution imaging due to the microfluidic channel underneath the chamber. To address these common limitations in microfluidic drug screening systems, we establish a reconfigurable microfluidic building block platform (Figure 1B). By introducing reconfigurable interfaces with plug-and-play microfluidic building blocks, the platform possesses the advantages of both microfluidics (e.g., multiplexing, flow control, and emulsion and chemical gradient generation) and high-throughput drug screening instruments (e.g., compound libraries and microplate readers and dispensers). We demonstrate this versatile platform for implementing the COC expansion and maturation assays for screening nonhormonal contraceptive compounds.

Materials and methods

Fabrication of the building block platform

The multilayer microfluidic platform comprises acrylic plates, double-sided tapes, membrane filters, and silicone rubber interconnects. For all layers, the acrylic layer and double-sided tape were patterned using a laser machining system (VLS 3.50 model, Universal Laser Systems) (Figure 2A). The silicone rubber interconnects were created by a mixture of

polydimethylsiloxane (PDMS) and Dragon Skin at a 1:1 ratio [16]. The silicone rubber had a high tear strength for the reversible and robust connections between building blocks. The mold for the interconnect was created by laser-machining of acrylic plates and double-sided tapes. The fluid passages were created by a biopsy puncher (0.2 cm in diameter). The silicone rubber layer and double-sided tapes were attached after plasma treatment (Harrick Plasma Cleaner PDC-1) for 5 minutes [17]. The silicone rubber interconnects were designed to be 1.2 times larger than the well size to create a tight seal between the layers (Figure 2C). Specifically, the inner diameter of the well was 0.5 cm, and the outer diameter of the interconnect was 0.6 cm. The middle layers were fabricated by assembling a membrane between two acrylic carriers with laminated double-sided tapes (Figure 2C). Figures 2D-E show examples of the top, middle, and bottom layers of the platform. Figure 2F shows an example of an integrated platform with an emulsion generator, a gradient generator, branching microchannels, and a pumpless flow controller. A transwell device was also designed and fabricated using the same method (Supplementary Figure S1).

Reagents and materials

The PDMS (Sylgard 184) was produced from Dow Corning, and the Dragon skin (10 MEDIUM) was obtained from SMOOTH-ON. The laminated hydrophilic polycarbonate track etch (PCTE) membrane with 30 µm pore size was purchased from Sterlitech. The nylon mesh filters with 10 and 20 µm pore size were purchased from Spectrum Labs for the pumpless flow controller building block experiment. The clear acrylic plates with 1.5 mm and 3 mm thickness were purchased from SIBE-R Plastic Supply^{SM}. The double-sided tape was 3M™ 9965 double-coated polyester diagnostic tape. Oxygen plasma treatment was performed by Harrick Plasma Cleaner PDC-1.

Cumulus-oocyte complex expansion and maturation assay

The COC expansion and maturation assay was applied for demonstrating the reconfigurable microfluidic building block platform. Mice were injected with pregnant mare serum gonadotropin (PSMG) on days 18–20 and were sacrificed 46 h post injection. Ovaries were poked with syringe needles to rupture the follicles and release COCs, which were transferred via mouth pipetting into a clean dish containing minimum essential medium α (MEMα), bovine serum albumin (BSA), 4-(2-hydroxyethyl)-1-piperazineethanesulfonic acid (HEPES), and 1 µM Milrinone to prevent early maturation. The device was rinsed with MilliQ water and allowed to dry.

Ultraviolet sterilization was performed for 10 min per side of multiwell array. Then, 25 µl of the COC expansion medium with MEMα, BSA, HEPES, epidermal growth factor (EGF, 10 ng/ml), and fetal bovine serum (FBS, 5%) was added to positive control wells. Negative control wells (no expansion) contained maturation medium without EGF and wells with maturation medium containing a known inhibitor of expansion, N,N,N′,N′-tetrakis-(2-pyridylmethyl)-ethylenediamine (TPEN, 10 µM). Thereafter, the device was placed in an incubator at 37°C with 5% O_2 and 5% CO_2 to attain equilibrium. Before addition to the device, COCs were transferred to a wash plate containing MEMα, BSA, and HEPES and incubated for 5 min. The COCs were then transferred in groups of five via pipette together with 1 µL of the medium. A gas-permeable membrane (Breathe-Easy® sealing membrane) was placed over the top of the multiwell array, and the device was set on a solid base plate to prevent contamination. The sample was incubated overnight at

37 °C with 5% O_2 and 5% CO_2. After expansion, the COCs were imaged with brightfield optics and captured with a CCD camera. The area of the expanded COC was determined using cellSens software (Olympus Microscopes, Center Valley, CA). To allow high resolution imaging of the oocyte development, cumulus cells were removed from the oocytes with hyaluronidase in the microfluidic device. Washing was performed using the medium. Then, 6 µL Hoechst and 2 µL Actin Green stain were added for in situ fluorescence staining. The mixture was incubated for 20 min. Excess dyes were removed by flushing the device with 40 mL of the medium before fluorescence microscopy. Animals were used according to the Guide for the Care and Use of Laboratory Animals in addition to review and approval by the Institutional Animal Care and Use Committee at The Pennsylvania State University.

Imaging and data analysis

The device was initially imaged using the 10x objective with bright field optics. Using the cellSens dimension software an overview region was imaged using the 4x objective, before specific regions of interest were selected and imaged at 10x. 10 µL of stain mix (1.2 mL MEMα + BSA + HEPES, then add 6 mg Hyaluronidase and filter before adding 6 µL Hoechst and 2 µL Actin Green stain) was added to each droplet and allowed to incubate for 20 minutes. Oocytes were denuded and the excess stain was removed by flushing the device with 40 ml of MEMα + BSA + HEPES which had been equilibrated to 37°C with 5% O_2 and 5% CO_2 in the incubator. The denuded oocytes were then imaged with a 20x objective under brightfield, DAPI, and green fluorescent protein channels, using a z-stack which takes two images 10 µm apart to allow for clear visualization of both the upper and lower bound of the oocyte. The expansion areas were analyzed by ImageJ. Two pairs of multiple comparisons between positive control (n=44 COC), negative control (n=48 COC), and TPEN (n=45 COC) were performed by ANOVA and Tukey's post-host test ($P<0.01$). For characterizing the building blocks, polynomial regressions of the experimental data were achieved by the MyCurveFit tool. The diffusion calculation was performed by MATLAB.

Result and Discussion

Reconfigurable microfluidic design

Our overall design concept centers around a multiwell array. To take advantage of various microfluidic operations, the multiwell array is designed to interface with various building blocks below and above (Figure 1B). The reconfigurability is enabled by the silicone rubber interconnects created by mixing Dragon Skin and PDMS. PDMS creates a strong adhesion with the double-sided type after plasma treatment. Dragon Skin is introduced to obtain a high tear strength for reversible, leak-free fluidic connections by press fitting the silicone interconnects into the wells. The top layer can be replaced with various microfluidic building blocks, such as 3D branching channels for enzyme loading and cumulus cell washing (Figure 2B). The top layer can also be removed for direct interfacing with high throughput drug screening equipment, such as multichannel pipettes and liquid handlers, and compound libraries (Supplementary Movie 1). The middle layer comprises an array of microwells with an embedded membrane filter to facilitate medium exchange, enzymatic removal of cumulus cells, and fluorescence staining (Figure 2E). The bottom layer can be a reservoir for waste collection, a solid base plate for COC culture and incubation, and an optical thin film for high resolution imaging

(Figure 2D). Other compatible interfaces include microplate reader carriers, transwell devices for cell migration assays, and a heating block for temperature control. Figure 2F shows an 8 by 16 system assembled with branching channel building blocks, a chemical gradient generator, a pumpless flow controller, and an emulsion generator.

Branching microchannel building blocks

Liquid dispensing to all wells is often required in drug screening procedures. A 3D branching microchannel building block was designed for flow splitting and liquid dispensing (Figure 2A-B). The 3D branching microchannels can be applied for steps requiring uniform liquid dispensing in the COC assay, including washing, enzyme loading, and fluorescence staining. In particular, symmetric channel geometry (e.g., a 1-to-4 splitter) was chosen to ensure uniform flow resistance in all fluid paths. The 3D geometry allowed multiple stages of splitting (e.g., 1-to-8 and 1:16 splitters) with uniform flow resistance.

Interchangeable microfluidic building blocks were assembled on the multiwell array, and the building blocks were loaded with water and food dyes to visualize the channels. Loading of reagents can also be performed directly using a multichannel pipette or a single channel pipette, allowing flexible operation for various drug screening applications. For instance, a 1-to-168 splitter were employed to transfer different dye solutions for illustrating the washing and enzyme loading steps in the COC assay (Supplementary Movie 1). After on-chip washing, the top layers of the building blocks were detached, and the multiwell arrays were filled with different dyes.

Gradient generator building blocks

Applying a range of concentrations is required to evaluate the dose dependent effect of a reagent and to determine the optimal drug concentration. A gradient generator with two inlets and symmetric branching/dividing channels was designed to generate chemical gradients (Figure 3A). The chemical diffuses through the interface of laminar flow and generates a range of chemical concentrations. By adjusting the channel design and flow rate, it is possible to create various concentration gradients (e.g., linear and non-linear) [18]. The gradient generator building blocks can also be applied to create multiple drug combinations for screening potent drug cocktails.

The chemical gradient building block was regulated by adjusting the flow rate and the degree of diffusion in the channel. Since all zig-zag channels have the same dimensions and the same flow resistance, the flow in each channel can be determined by considering the equivalent circuit (Supplementary Figure S2). The degree of diffusion depends on the flow rate and the diffusion time available in the zig-zag channel. The process can be modeled as one-dimensional diffusion of two laminar streams without convection using the Fick's second law:

$$\frac{dC}{dt} = D\frac{d^2C}{dx^2} \quad (1),$$

where *C* is the concentration and *D* is the diffusion coefficient. The solution follows the complementary error function:

$$C = \frac{1}{2}c_0 erfc\left(\frac{x}{2\sqrt{Dt}}\right) \quad (2),$$

where c_0 is the initial concentration. With a higher flow rate, the diffusion time will be shortened, and a lower degree of diffusion will occur [19].

To experimentally create a concentration gradient across multiple wells, a gradient generator building block was attached to the multiwell array and loaded with a dye solution (Figure 3B and Supplementary Movie 2). A microplate reader was applied to measure the chemical concentration by measuring the optical density (O. D.) at 510 nm in each well (Figure 3C). We also estimated the chemical gradient generated with a numerical calculation. In particular, the diffusion coefficient of the food dye for numerical calculation was 5.75×10^{-6} cm^2/s. The length of zig-zag channel was 27 mm, and the flow rate was 30 ml/min (flow speed 82-222 mm/s). The time required to pass the zig-zag channel was 0.12-0.32 s. Numerical calculation with equation (2) revealed that a high degree of diffusive mixing could be achieved after 0.1 s (Figure 3D). Based on the equivalent circuit model, an approximately linear gradient could be generated when the fluid streams were thoroughly mixed (Supplementary Figure S2). In agreement, a low flow rate (e.g., 30 ml/min) resulted in a sufficient diffusion time and a linear gradient. In contrast, when the flow rate was increased (e.g., 60 ml/min), a lower degree of diffusion resulted a non-linear (sigmoidal) chemical gradient.

Pumpless flow controller building blocks

A flow controller is useful when the procedure requires an adjustable flow rate (e.g., washing and medium exchange). Thus, we designed a pumpless flow controller building block that generates continuous flows independently. In this design, the flow is driven by hydrostatic pressure, and the flow resistance is regulated by incorporating a filter membrane. The relationship between the flow rate and the pressure difference can be estimated as

$$Q = \frac{\Delta P}{R_c + R_m} \quad (3),$$

where R_c and is the flow resistance of the channel and R_m is the flow resistance of the membrane, which can be approximated as

$$R_m = \frac{32\mu L_m}{\varepsilon A_m d_m^2} \quad (4),$$

where μ is the viscosity of the fluid, L_m is the thickness of the membrane, ε is the porosity, A_m is the cross-sectional area, and d_m is the pore diameter [20]. By controlling the pore radius and the percentage of the open area of the membrane, the flow rate can be adjusted. For example, a small pore size creates a large flow resistance and creates a small flow rate.

A four-channel reagent-loading device was designed to demonstrate the concept of the pumpless flow controller (Figures 4A-B and Supplementary Movie 3). The flow was driven by the hydrostatic pressure of the reservoir. When the physical (on-off) valve was opened, a continuous flow was generated. We measured the reservoir heights and converted the reservoir heights into hydrostatic pressure (mbar). As expected, the flow rate increased with the hydrostatic pressure and decreased with the pore size. The pore size of the membrane provided an easy way for controlling the flow resistance. Using the device, the flow rate could be adjusted for 500 folds (Figure 4C).

Emulsion generator building block

Multiphase microfluidic systems are often applied for fabricating microcapsules or microgels for drug delivery, digital assays, and single-cell analysis [21-22]. Figure 6A shows a microfluidic building block design with a crossflow emulsion generator. By altering the flow rate and the channel geometry, the properties of the emulsion can be regulated depending on the Capillary number [23]. Theoretical analysis predicts the size of the droplet follows a power-law relationship:

$$\frac{l}{a} = \alpha(\frac{Q_w}{Q_o})^{\beta} \quad (6)$$

where l is the diameter of the droplet, a is the half of the channel width, Q_w is the flow rate of water and Q_o is the flow rate of oil phase. α and β are constants dependent on the geometry and fluid properties.

We demonstrated emulsion generation with a building block platform (Figure 6B and Supplementary Movie 4). In our experiment, the flow rate of the aqueous phase (water) was fixed at 0.25 ml/min. The droplet size decreased as the flow rate of the oil phase increased (Figure 6C). ImageJ was used to analyze the droplet diameter under different flow rates of oil (Figure 6C). Curve fitting revealed a scaling power exponent of 0.55 in our experimental setup. Our results suggest the droplet size can be regulated by modifying the flow rate in the building block.

Overall, these results illustrate our building block platform is compatible with various microfluidic operations. This compatibility is beneficial for implementing diverse biochemical protocols and supports the potential of the reconfigurable platform for various drug screening tests and biochemical assays.

High-throughput nonhormonal contraceptive screening

The capability of the reconfigurable microfluidic platform for contraceptive screening was demonstrated by performing the COC expansion and maturation assay (Figure 6). In particular, an 8 by 8 (i.e., 64 wells) device was used for testing the COC expansion and maturation assay. Reagent addition including test compounds, oocyte incubation, enzyme loading, fluorescence staining, and fluorescence microscopy were performed on the platform with different building blocks (Figure 6A). The first step of the assay was overnight incubation of COCs (3-4/well) with expansion media (MEM-alpha, 3 mg/ml BSA, 5% FBS and EGF 10 ng/ml) alone, with test compound (TPEN, 10 uM) or no EGF (negative control). TPEN is a known inhibitor of COC maturation and expansion [17] and was used to demonstrate that the device and procedure could detect inhibition of cumulus expansion. The test media and COCs were loaded randomly onto the open wells of the microfluidic building block with a multichannel pipette. The multiwell array was covered by a gas-permeable membrane and set on a solid base plate during incubation at 37°C for 12-14 hours. After incubation, the solid plate was then replaced by an optical thin film for imaging COC expansion with an inverted IX83 microscope (Olympus) (Figure 6B-C). After capturing expansion images, media with 3 mg/ml Hyaluronidase was flushed through the wells with the 3D branching channel and a bottom reservoir for removal of cumulus cells. The pore size (10 μm) was chosen for washing away the cumulus cells but not the oocytes. After cumulus cells were removed, media containing the DNA dye, Hoetchst (60 mg/ml), and 1X actin dye (CellMask Green Actin Tracking Stain, Invitrogen) was added. After on-chip washing, the bottom reservoir was replaced with the optical thin film. Then, the oocytes were imaged by epifluorescent microscopy (Figure 6F-G).

The expansion area of individual COCs were measured on brightfield images using ImageJ software (NIH). As shown in Figure 6B-D, the expansions of negative control and TPEN treatment were reduced significantly compared to the positive control. The area measurements of expanded COC (PC, positive control (n=44 COC); NC, negative control (n=48 COC) and TPEN (n=45 COC) indicated significant differences by ANOVA and Tukey's post-hoc test (Figure 6E). During normal oocyte maturation, asymmetric division proceeds with the formation of small and spherical polar bodies. As shown in the control case (Figure 6F), the presence of the polar body indicated successful maturation [24-25]. In contrast, TPEN disrupted the asymmetric division and inhibited the formation of a polar body (Figure 6G). Furthermore, an experiment was performed to determine if well location influenced expansion across an 8X8 plate. As shown in figure 6H, expansion proceeded normally across the plate and was significantly different from negative non-expanded controls (Figure 6H). These results show the applicability of the platform for screening nonhormonal contraceptives.

Conclusions

This study reported a reconfigurable microfluidic building block platform of high-throughput drug screening, and nonhormonal contraceptive screening was demonstrated using the platform. Additional building blocks and layers (e.g., multiple cell and tissue types) can be incorporated into the platform to perform other contraceptive screening procedures. The scalability and adaptability of the building block platform hold the potential to revolutionize various drug screening tests and biochemical assays in the future.

Author Contributions

Conceptualization FD, PW, JL; Investigation JL, CL; Writing JL, PW.

Conflicts of interest

"There are no conflicts to declare".

Acknowledgements

This work is supported by the Bill and Melinda Gates Foundation Grand Challenge program (INV-003768).

References

1 J. Santelli, R. Rochat, K. Hatfield-Timajchy, B. C. Gilbert, K. Curtis, R. Cabral, J. S. Hirsch, L. Schieve and Unintended Pregnancy Working Group, *Perspectives on sexual and reproductive health*, 2003, 94-101.

2 L. J. Burrows, M. Basha and A. T. Goldstein, *the journal of sexual medicine*, 2012, **9**, 9, 2213-2223.

3 S. Christin-Maitre, *Best practice & research Clinical endocrinology & metabolism*, 2013, **27**, 1, 3-12.

4 M. C. Peluffo, J. Stanley, N. Braeuer, A. Rotgeri, K.-H. Fritzemeier, U. Fuhrmann, B. Buchmann, T. Adevai, M. J. Murphy, M. B. Zelinski, B. Lindenthal, J. D. Hennebold and R. L. Stouffer, *Human reproduction,* 2014, **29.7**, 1400-1412.

5 X. Tian, K. Anthony and F. J. Diaz, *Biological trace element research*, 2017, **176**, 2, 374-383.

6 L. Curci, G. Carvajal, V. Sulzyk, S. N. Gonzalez and P. S. Cuasnicú, *Frontiers in cell and developmental biology*, 2021, **9**, 686461.

7 K. Jiang, J. Zhang, Y. Huang, Y.Wang, S. Xiao, M. K. Hadden, T. K. Woodruff, and J. Sun, *Proceedings of the National Academy of Sciences*, 2021, **118**, 28.

8 B. Zhang, A. Korolj, B.F.L. Lai and M. Radisic, *Nature Reviews Materials*, 2018, **3**, 8, 257-278.

9 A. G. Toh, Z. P. Wang, C. Yang and N. T. Nguyen, *Microfluidics and nanofluidics*, 2014, **16**, 1, 1-18.

10 J.-L. He, A.-T. Chen, J.-H. Lee and S.-K. Fan, *International journal of molecular sciences*, 2015, **16**, 9, 22319-22332.

11 H. Li, E. Shkolyar, J. Wang, S. Conti, A. C. Pao, J. C. Liao, T.-S. Wong and P. K. Wong, *Science advances,* 2020, **6**, 21, eaba8535.

12 L. Rosenfeld, T. Lin, R. Derda and S. K. Tang, *Microfluidics and nanofluidics*, 2014, **16**, 5, 921-939.

13 G. Du, Q. Fang and J. MJ den Toonder, *Analytica chimica acta*, 2016, **903**, 36-50.

14 P. Cui and S. Wang, *Journal of pharmaceutical analysis*, 2019, **9**, 4, 238-247.

15 H. Li, T. Garner, F. J. Diaz and P. K. Wong, *Small*, 2019, **15**, 28, 1901910.

16 L. Wei, W. Li, E. Entcheva and Z. Li, *Lab on a Chip*, 2020, **20**, 21, 4031-4042.

17 S. Hassanpour-Tamrin, A. Sanati-Nezhad and A. Sen, *Scientific Reports*, 2021, **11**, 1, 1-12

18 N. L. Jeon, S. K. W. Dertinger, D. T. Chiu, I. S. Choi, A. D. Stroock, and G. M. Whitesides, *Langmuir*, 2000, **16**, 22, 8311-8316.

19 B. J. Kriby, *Micro-and nanoscale fluid mechanics: transport in microfluidic devices. Cambridge university press*, 2010.

20 Z. Chen, J. Zilberberg and W. Lee, *Biomedical Microdevices*, 2020, **22**, 3, 1-10.

21 C.-X. Zhao, *Advanced drug delivery reviews*, 2013, **65**, 11-12, 1420-1446.

22 H. N. Joensson and H. A. Svahn, *Angewandte Chemie International Edition*, 2012, **51**, 49, 12176-12192.

23 T. Ward, M. Faivre, M. Abkarian, and H. A. Stone, *Electrophoresis*, 2005, **26**, 19, 3716-3724.

24 X. Tian, and F. J. Diaz, *Endocrinology*, 2012, **153**, 2, 873-886.

25 X. Tian, and F. J. Diaz, *Developmental biology*, 2013, **376**, 1, 51-61.

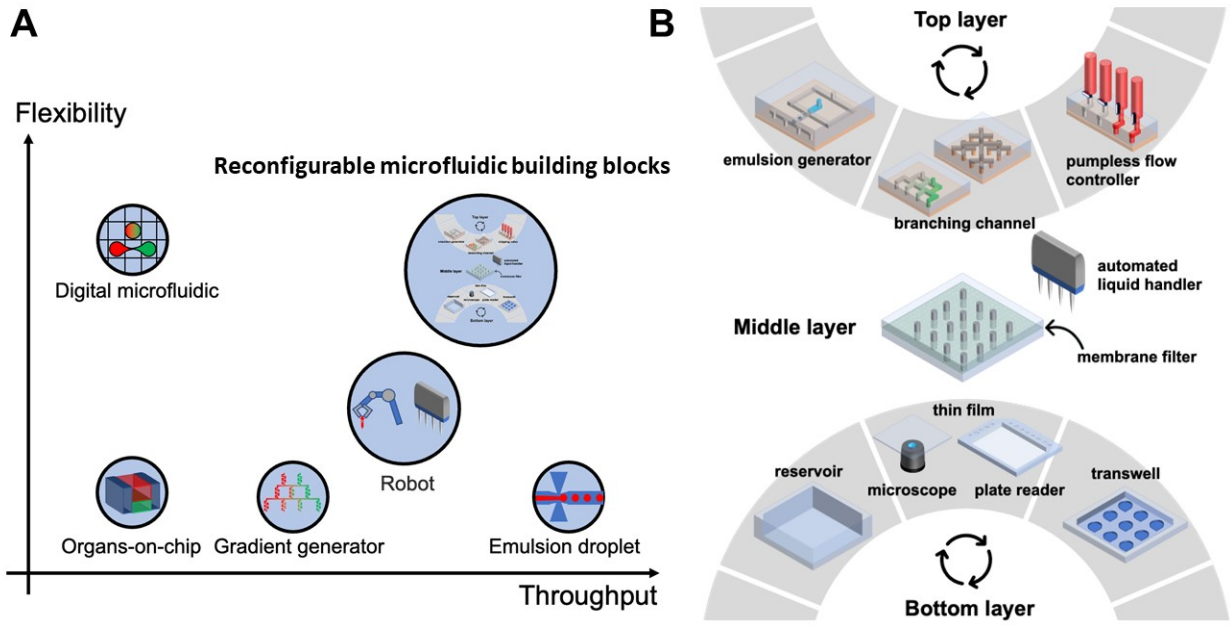

Fig. 1 A) Comparison of microfluidic and liquid handling platforms for drug screening. B) Schematic of the reconfigurable microfluidic building block platform. The platform consists of three layers. The top layer is an interchangeable layer for microfluidic manipulation and can be mixed and matched with different building blocks. The middle layer is an array of microwells with an embedded membrane filter to facilitate liquid exchange. The microwell array can also directly interface with automated liquid handlers and plate readers. The bottom layer is also interchangeable for waste collection, imaging, and incubation.

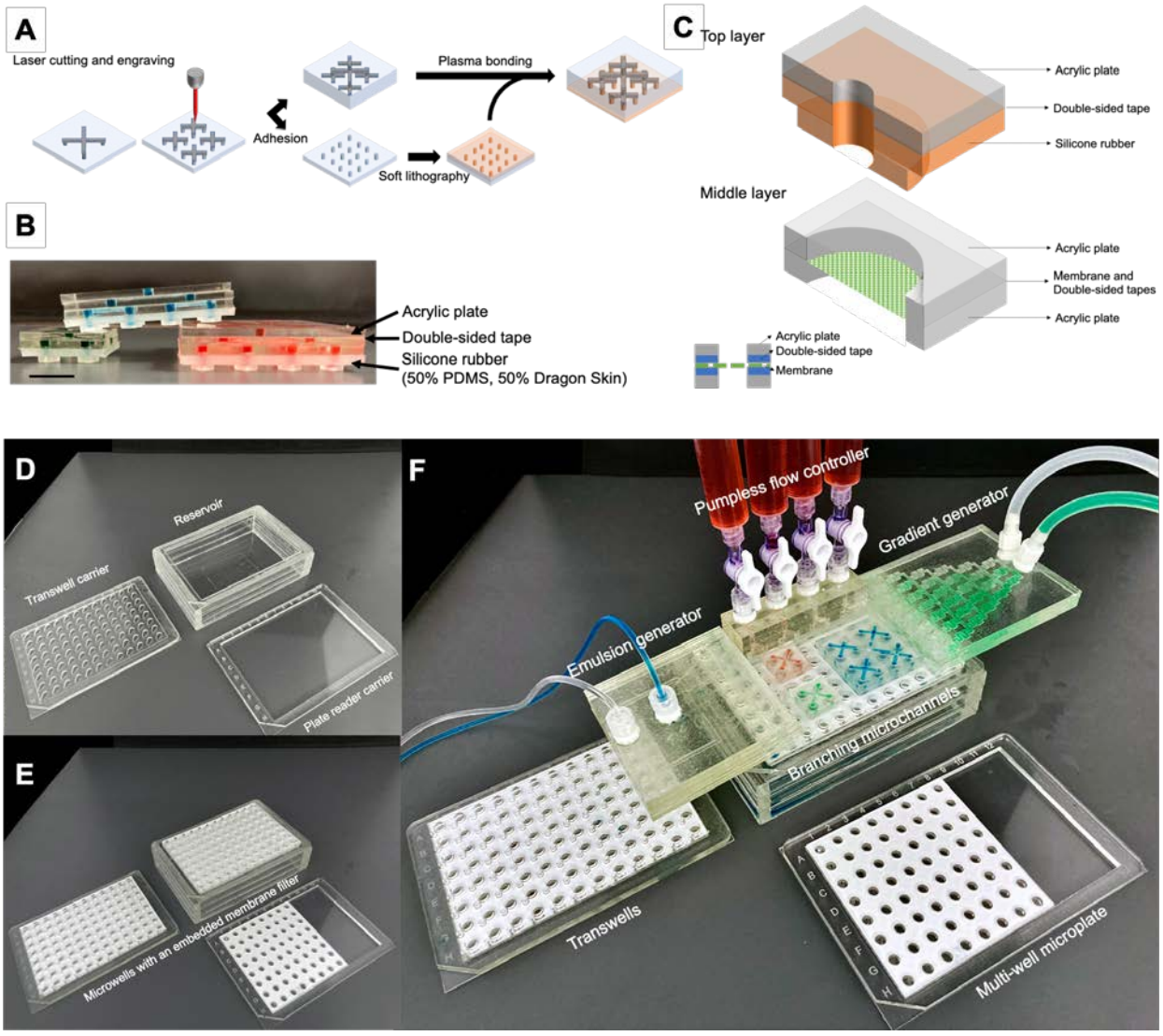

Fig. 2 A) Fabrication and integration of microfluidic building blocks. B) Top layer of microfluidic building blocks. Scale bars, 1 cm. C) The interface design of top layer and middle layer. D) Bottom layer of microfluidic building blocks. E) Middle layer of microfluidic building blocks (microwells with an embedded membrane filter) assembled on the bottom layer. F) Example of an integrated microfluidic building block platform with an emulsion generator, a pumpless flow controller, branching channels, and a gradient generator assembled on the middle layer.

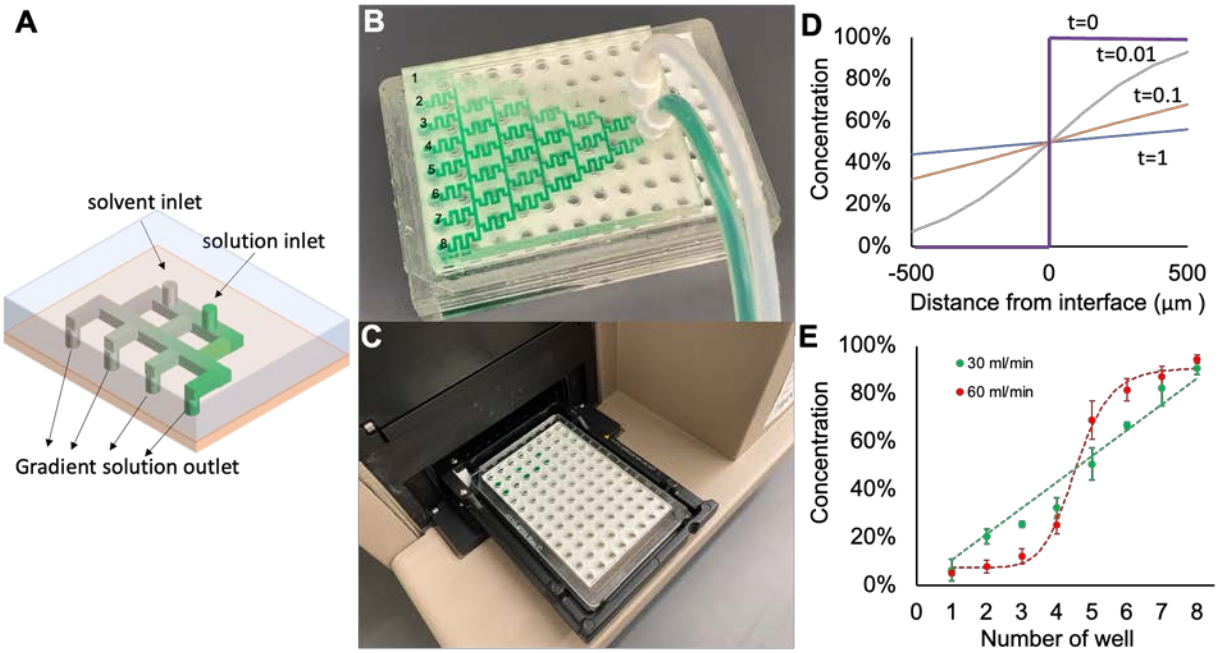

Fig. 3 A) Schematic of the gradient generator building block for loading drugs across multiple wells. B) Visualization of gradient generation with a green dye and DI water. C) The microwell layer (middle layer with an embedded membrane) was inserted into a microplate carrier. The chemical gradient was characterized by measuring the absorbance using a microplate reader. D) Numerical analysis of the chemical gradient with various levels of diffusion in the channel. E) Experimental characterization of the chemical gradients generated by different flow rates. Data represent mean ± standard deviation (n = 3). The images are representative of three independent experiments.

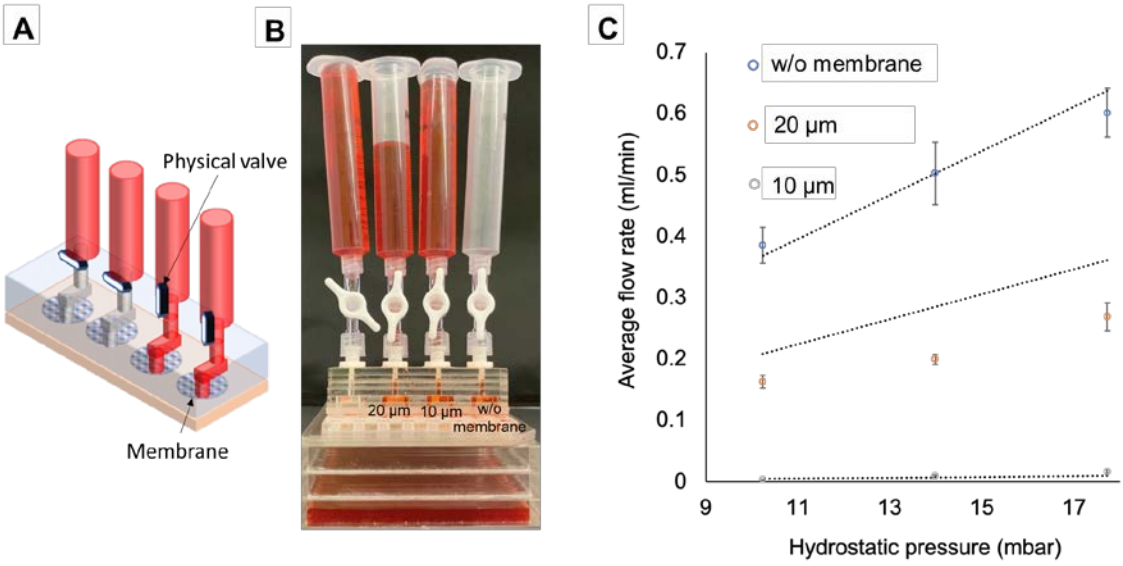

Fig. 4 A) Schematic of the pumpless flow controller building block for medium exchange and washing steps. Hydrostatic pressure drives a continuous flow into the well. The flow rate is controlled by the hydrostatic pressure and flow resistance created by the membrane. A physical value is also incorporated for on-off control. B) Image of the pumpless flow controller. C) Flow rate control with the hydrostatic pressure and membrane porosity. Data represent mean ± standard deviation (n = 3). The image is representative of three independent experiments.

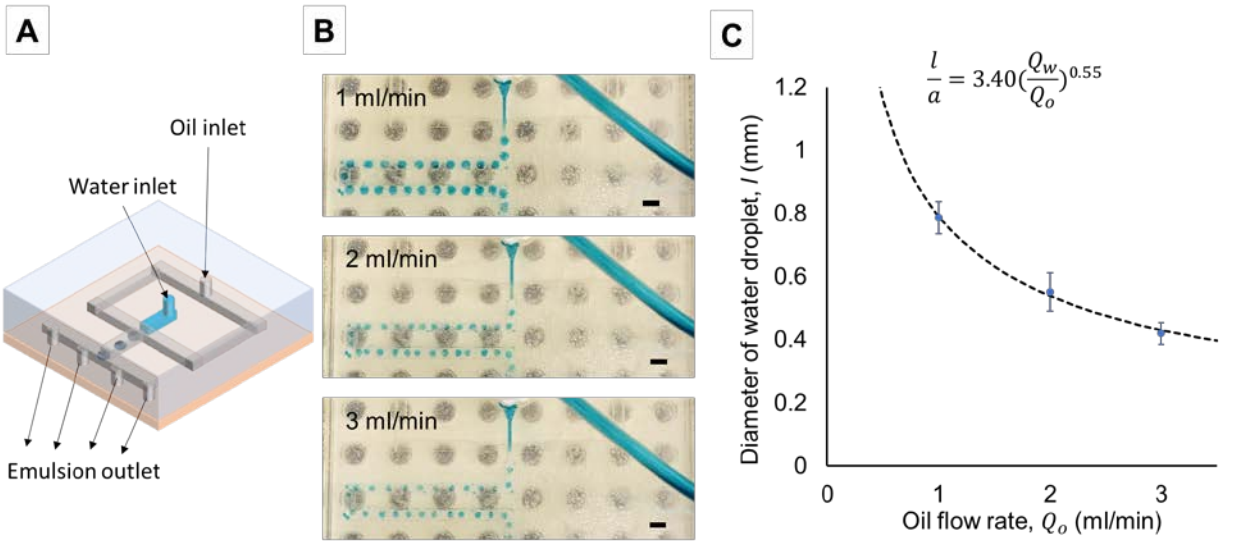

Fig. 5) A) Schematic of the emulsion generator building block for creating water-in-oil emulsions. B) Images of emulsion generation at different flow rate of the oil phase. The flow rate of the water phase was kept constant (0.25 ml/min). The droplet size decreased as the continuous phase flow rate increased. Scale bars, 2 mm. C) Droplet size measurement under different continuous phase flow rate. Data represent mean ± standard deviation (n = 6).

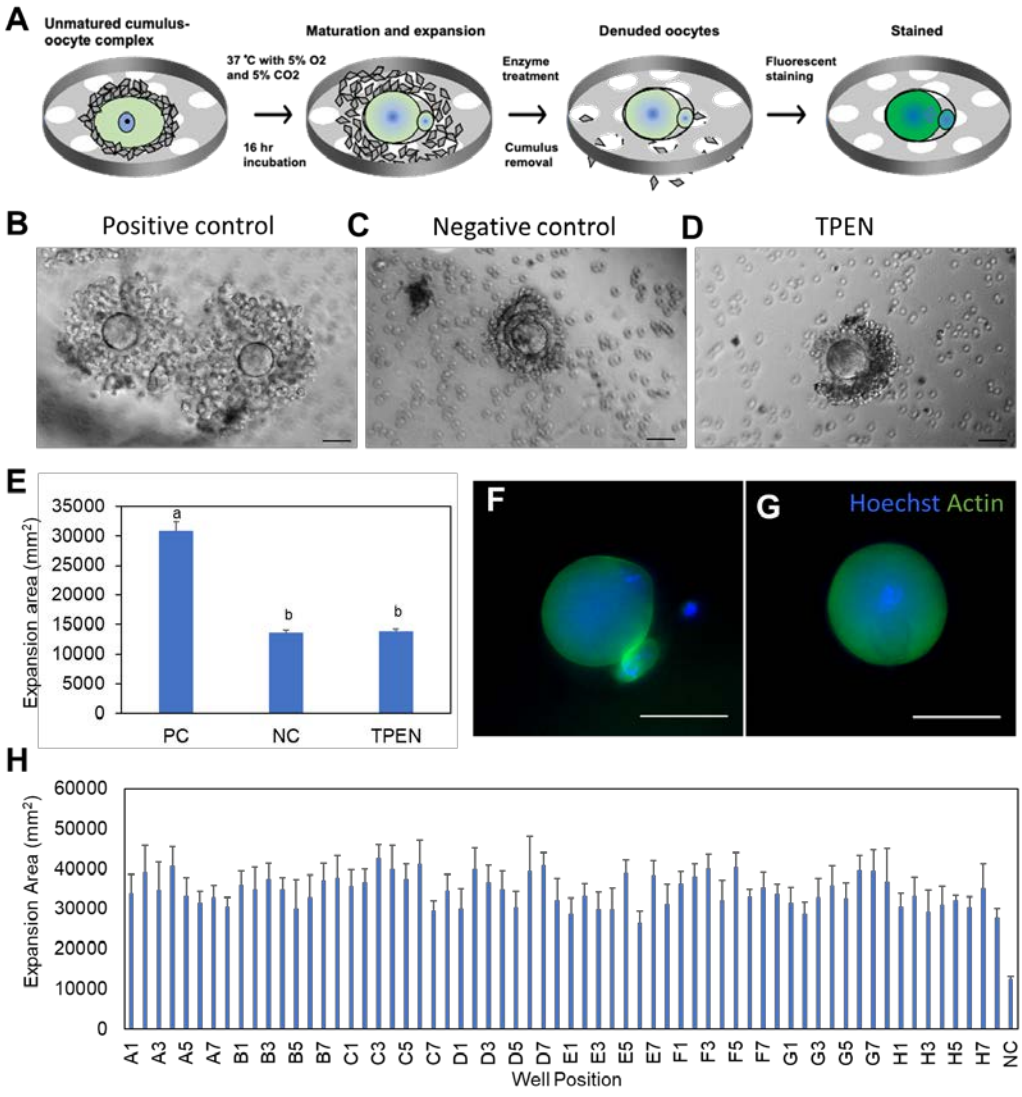

Fig. 6 A) Major steps of the on-chip COC maturation and expansion assay. Unmatured COCs were incubated with test compounds overnight. The expansion of COCs was imaged with brightfield microscopy. Cumulus cells were then removed enzymatically and washed away through the membrane. The denuded oocytes were then stained, washed, and imaged by fluorescence microscopy. B) Expansion of the COC after overnight incubation in positive control group. C) No expansion in negative control group without EGF. D) No expansion in COC treated with TPEN (10 μM). E) Area measurements of expanded COC (PC, positive control (n=44 COC); NC, negative control (n=48 COC) and TPEN (n=45 COC). Different subscripts indicate significant differences by ANOVA and Tukey's post-hoc test, $P<0.01$. F) Fluorescence staining of denuded oocytes with a polar body. G) Fluorescence staining of denuded oocyte without a polar body indicative of arrest at metaphase I of meiosis. DNA (blue), Actin (green). All scale bars are 50 μm. H). Area

of expanded COC across an entire plate compared to unexpanded controls. Area of all expanded COC (n=3-6 COC/well) were significantly different from negative control (NC), $P<0.05$.